

# Far-field single nanoparticle detection and sizing: supplementary material

**NAN ZHANG,<sup>1</sup> ZHIYUAN GU,<sup>1</sup> SHUAI LIU,<sup>1</sup> YUJIE WANG,<sup>1</sup> SHUAI WANG,<sup>1</sup>  
ZONGHUI DUAN,<sup>1</sup> WENZHAO SUN,<sup>1</sup> YUN-FENG XIAO,<sup>2,3</sup> SHUMIN XIAO,<sup>1,4</sup> AND  
QINGHAI SONG<sup>1,\*</sup>**

<sup>1</sup>State Key Laboratory on Tunable Laser Technology, Ministry of Industry and Information Technology Key Laboratory of Micro-Nano Optoelectronic Information System, Shenzhen Graduate School, Harbin Institute of Technology, Shenzhen 518055, China

<sup>2</sup>State Key Lab for Mesoscopic Physics and Department of Physics, Peking University, Beijing, China

<sup>3</sup>e-mail: yfxiao@pku.edu.cn

<sup>4</sup>e-mail: Shumin.xiao@hit.edu.cn

\*Corresponding author: qinghai.song@hit.edu.cn

Published 20 September 2017

This document provides supplementary information to “Far-field single nanoparticle detection and sizing,” <https://doi.org/10.1364/optica.4.001151>.

<https://doi.org/10.6084/m9.figshare.5328958>

## I. Methods

### A. Numerical Calculation

Because the thickness of microdisk is around 5 times smaller than its in-plan size, we thus simplified the microdisks into two-dimensional objects by using the effective refractive indices  $n$ . Then, the wave equations for transverse magnetic (TM, with  $E$  perpendicular to the plane) polarized modes  $E_z(z, y, t) = \psi(x, y)e^{-i\omega t}$  can be replaced by the scalar wave equation:

$$-\nabla^2 \psi = n^2(x, y) \frac{\omega^2}{c^2} \psi$$

where  $\omega$  is the angular frequency and  $c$  is the speed of light in vacuum.

We numerically computed the TM polarized resonances by solving the FEM with RF module in Comsol Multiphysics 3.5a. The cavity shape is defined using AutoCAD and imported into the software. A perfect matching layer is used more than 20  $\mu\text{m}$  away from the boundary of limaçon-spiral photonic molecule to fully absorb the outgoing waves and mimic the infinitely large space. Then complex eigenfrequencies ( $\omega$ ) can be obtained and then are normalized with  $kR = \omega R/c$ . Here  $c$  is the speed of light in vacuum.

### B. Fabrication

The limaçon-spiral photonic molecule is fabricated in a dye doped SU8 film on a silicon wafer. The thickness of SU8 film is around 1.9  $\mu\text{m}$  and the concentration of dye is 8% in weight. Then 300nm PMMA film is spin-coated onto the film and baked at 160  $^\circ\text{C}$ . The cavity boundaries are defined with electron-beam lithography (Raith E-line) and developed in MIBK for 50 second. Then 100 nm  $\text{SiO}_2$  film was deposited by electron-beam evaporation and lifted off in remover PG for 8 hours. Using the  $\text{SiO}_2$  patterns as mask, the microdisks are fabricated by two steps of ICP etching. The first step uses  $\text{O}_2/\text{Ar}$  to etch the dye doped SU8. The second step is an isotropic etching of silicon to form the pedestal underneath the microdisk. The size of pedestal is around 1 micron, which is small enough to exclude all the influences to high Q resonances.

### C. Single Nanoparticle Transferring

The nanoparticle has been attached to the side of limaçon microdisk with a tapered fiber. Basically, the diluted solution of polystyrene spheres is dropped onto the tapered fiber and the nanoparticles are well distributed along the tapered fiber. By injecting a He-Ne laser into tapered fiber, the positions of nanoparticles can be clearly seen from the scattering light and then the microdisk is moved close and attach to the nanoparticle with a three-dimensional translation stage.

## II. Optical Measurement Setup

The experimental setup is shown in Fig. S1.

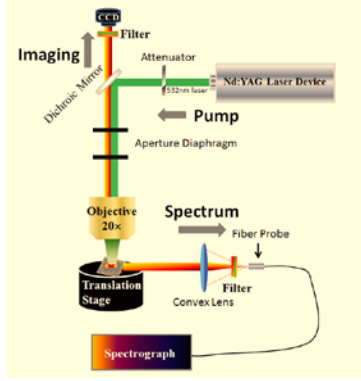


Fig. S1. Setup for measuring the photoluminescence and laser emissions from the limaçon-spiral photonic molecule.

In the lasing experiment, the samples were mounted onto a three-dimensional translation stage under a rotating translational platform and excited by a pulsed frequency doubled Nd:YAG laser (532 nm, 7 ns, 10 Hz). The pump light was focused onto the top surface of the samples through a 10x objective lens and the beam size was adjusted to  $\sim 45$  micron, which can well cover on the microdisk. The emitted lights were collected by a convex lens and coupled to a CCD (Princeton Instruments, PIXIS UV enhanced CCD) coupled spectrometer (Acton SpectroPro s2700) via a multimode fiber. The fluorescent microscope images were recorded by a CCD camera behind a long-pass filter.

## III. Laser Spectra of the Limaçon Microdisk and Limaçon-Spiral Photonic Molecule

### A. Laser Action in the Limaçon Microdisk

The boundary shape of limaçon cavity is defined by the equation  $\rho(\theta) = R(1 + \epsilon \cos(\theta + \pi))$  in polar coordinates, where  $R$ ,  $\theta$ , and  $\epsilon$  are the radius, polar angle, and deformation parameters, respectively (see cavity shape in Fig. S2(a)). The ray and wave dynamics inside the microcavity have been thoroughly studied in literatures. While the Poincaré surface of section is dominated by the chaotic motions, high  $Q$  resonances can still be formed by wave localizations. Based on our previous experimental results, here we only considered the transverse magnetic (TM,  $E$  is perpendicular to the plane) polarization. Fig. S2(b) shows the  $Q$  factors of resonances in a limaçon cavity with  $R = 5 \mu\text{m}$ ,  $\epsilon = 0.4$ , and refractive index  $n = 1.56$ . We can see a series of high  $Q$  resonances have been formed. One example of field pattern is shown in Fig. S2(a). It is a 6-bounce resonance that is confined by wave localization. In high refractive index microcavity, the leakages of such high  $Q$  resonances follow the well-known unstable manifolds and generate unidirectional output in far field. In the low refractive index microcavity, as the critical line ( $\sin \chi = 1/n$ ) is very close to the main mode structure, the situation becomes a little bit different. As shown in Fig. S2(c), the counterclockwise (CCW) waves ( $\sin \chi > 0$ ) directly transmit out at  $\theta \sim \pi/2$  before they follow the unstable manifolds. Similarly, the clockwise (CW) waves leak at  $\theta \sim 3\pi/2$ . Due to the presence of mirror-reflection symmetry, the CW and CCW components are balanced (see Fig. S2(c)) and two directional emissions along  $\phi_{\text{FF}} = \pm 150^\circ$  can be formed in far field (see dashed line in Fig. 1(d)).

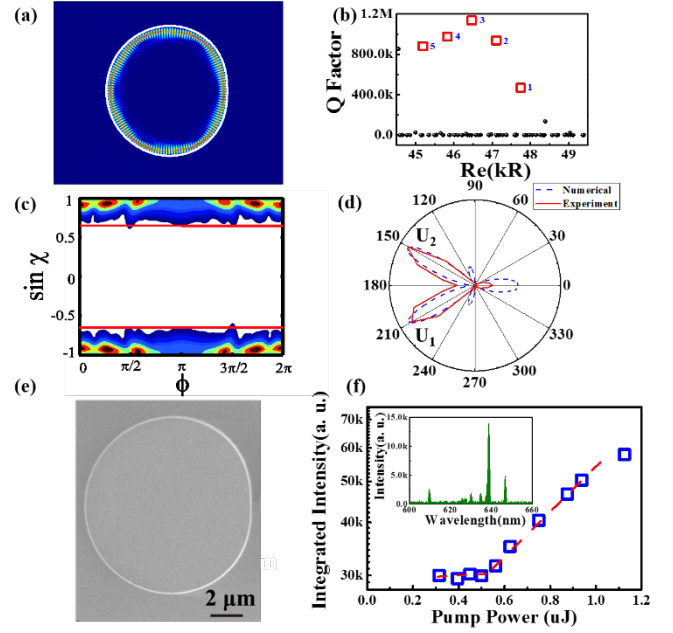


Fig. S2. Resonant and lasing properties of regular limaçon microdisk. (a) The resonant mode profile in the limaçon microdisk. The dashed line is the cavity boundary. (b) The calculated  $Q$  factors in limaçon microdisk. (c) and the dashed line in (d) are the Husimi map and the corresponding far field pattern of mode-2 in (b). (e) The top-view SEM image of the fabricated limaçon microdisk. (f) The output intensity as a function of pumping energy. The inset shows the lasing spectrum, and the corresponding far field pattern is plotted as solid line in (d).

To verify above analysis, we have fabricated dye-doped SU8 microdisks (refractive index  $n = 1.56$ ) with electron beam lithography and two-step inductively coupled plasma (ICP) etching. As shown in Fig. S2(e), the top-view scanning electron microscope (SEM) image of the microdisk can be well fitted with the limaçon equation with  $R = 5 \mu\text{m}$  and  $\epsilon = 0.4$ . Then the microdisk was optically excited under a homemade microscope and the corresponding laser characteristics were recorded (see Fig. S2(f)). When the pumping energy was low, the emission spectrum was a broad photoluminescence peak. And the output intensity increased slowly. Once the pumping density was above  $0.5 \mu\text{J}$ , periodically sharp laser peaks emerged and quickly dominated the spectrum. The mode spacing was around 8 nm, which matched the resonances along the cavity boundary well. Meanwhile, the integrated output intensity increased dramatically. All these phenomena confirmed the lasing actions. We also measured the polarization of these modes (see Fig. S3 below). Similar to the numerical calculation, the laser modes are TM polarized. When the pumping power was above threshold, bright spots could also be observed in the far field. These bright spots clearly showed the directional emissions of microdisk lasers. By rotating the translation stage, the far field distributions of microdisk lasers were recorded. As the solid line in Fig. S2(d), two emission beams at  $\phi_{\text{FF}} = \pm 150^\circ$  have been observed, consistent with the numerical results well.

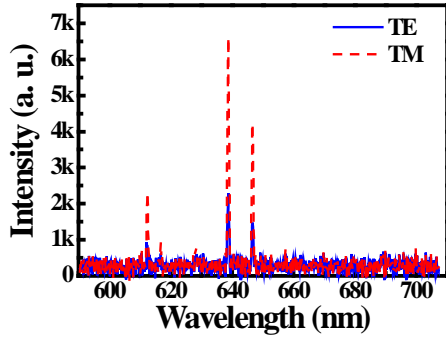


Fig. S3. Polarization spectrum of a single limaçon microdisk.

In Fig. S2(f), we show the output intensity as a function of the pump energy and a lasing spectrum. The detail spectra of the limaçon microdisk with different pump energies are shown in Fig. S4(a). With the increase of pumping power, we can see the transition from photoluminescence to lasing actions. Fig. S4(b) shows the high resolution spectrum around the threshold. The linewidth is around 0.04 nm, which is limited by our spectrometer.

In lasing experiment of single limaçon microdisk, due to the presents of mirror-reflection symmetry, the CW and CCW components are balanced and two directional emissions along  $\phi_{FF} = \pm 150^\circ$  can be formed in far field which is well matched with the numerical results. When we pumped the microdisk, there are two dominated modes. The far field angular distribution of the total emission has been shown in Fig. S2(d). Here we shown the detail experiment results. As shown in Fig. S5, the laser spectra consist of two lasing peaks, which are marked as Mode-1 and Mode-2. More than the total output emission far field pattern in Fig. S2(d), we have also summarized the individual lasing mode. The results are plotted in Fig. S5(c) and Fig. S5(d), respectively. We can see that the individual lasing modes have similar bi-directional laser emissions in far field patterns.

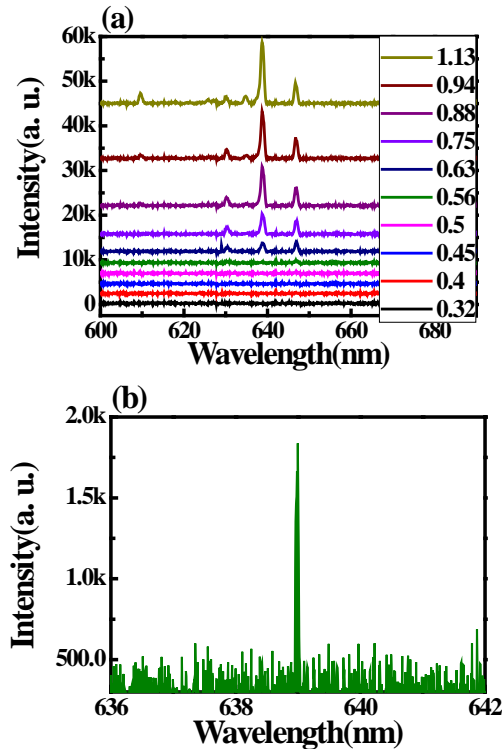


Fig. S4. (a) Detailed spectra at different pump energy. (b) The laser spectrum at laser threshold.

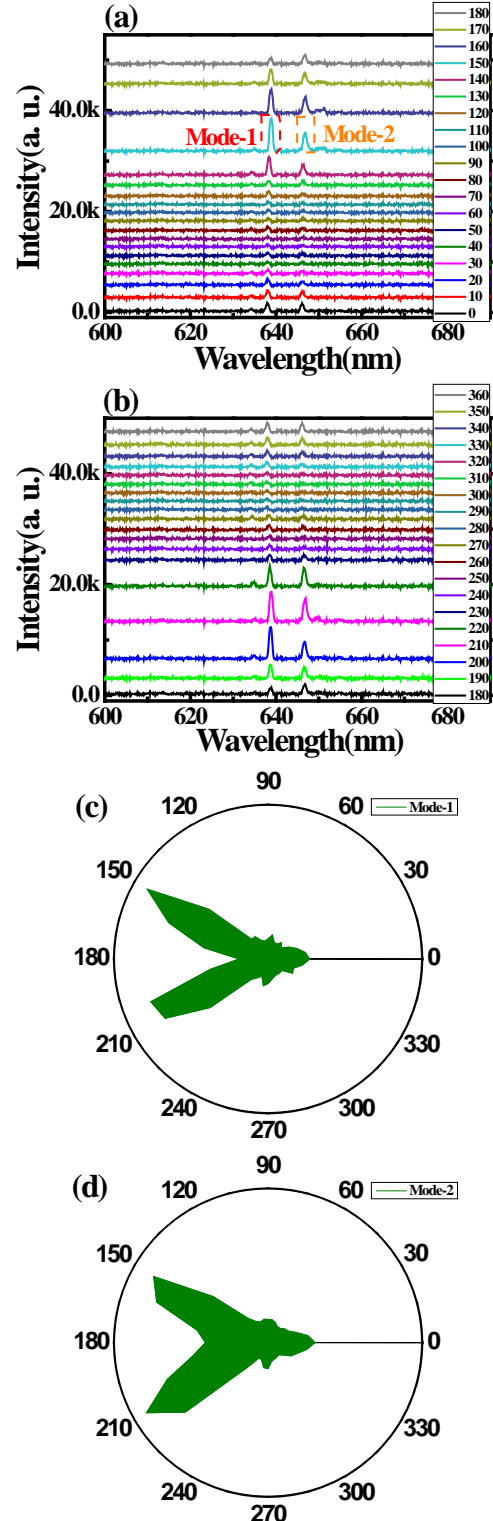


Fig. S5. (a) and (b) Detailed spectra of the limaçon microdisk at different collection angles. (c) and (d) are the far-field patterns of Mode-1 and Mode-2.

#### B. Laser Action in a Limaçon-Spiral and the Corresponding Far-Field Patterns

To verify the relationship between far field pattern and chirality, we studied the laser properties of limaçon-spiral photonic molecule. The threshold curve has been shown in Fig. 4, and the detailed

spectra with different pump energies are shown in Fig. S6. When the pumping power is low, the emission spectrum is relatively flat. This is because the spectrum is measured with high resolution grating. The broad photoluminescence is relatively flat in a small spectral range. With the increase of pumping power, narrow peaks appear and quickly dominate the emissions. The mode spacing in this figure is similar to the results in Fig. S4. Thus we know the lasing actions are still generated within the limaçon cavity even though a spiral microdisk has been placed close to it.

Fig. S7 shows the polarization of the emitted laser. We can see that the TM polarization is still much larger than the TE polarization. This result is consistent with the lasing actions in a single limaçon microdisk. Actually, for the polymer microdisks, we find that their main polarizations are all TM polarization with E perpendicular to the plane of microdisks.

Besides the observation of laser actions in the limaçon-spiral photonic molecule, it is more important and essential to detect far field pattern and to confirm the proposed mechanism. We then rotated the translation stage and recorded the laser spectrum at every 10 degrees. In Fig. 2, we showed the angular distribution of the emissions at far field pattern. Here we show the detailed laser spectra at different far-field angles in Fig. S8. We can see that almost all of the lasing modes have very close far field patterns.

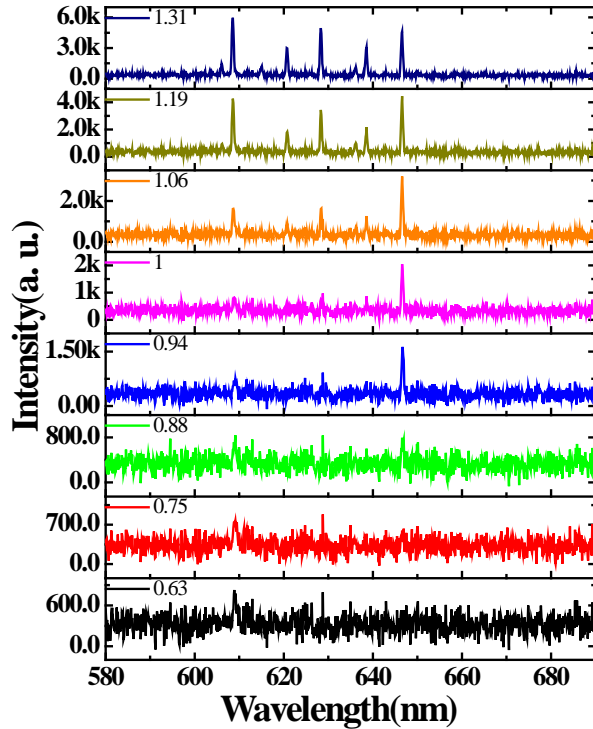


Fig. S6. Detailed spectra with different pump energies of the limaçon-spiral photonic molecule.

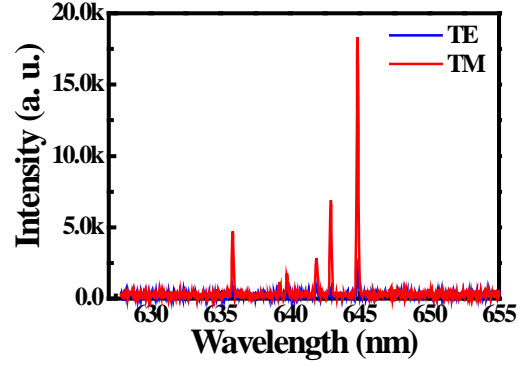


Fig. S7. Detailed spectra of the polarization of the limaçon-spiral photonic molecule.

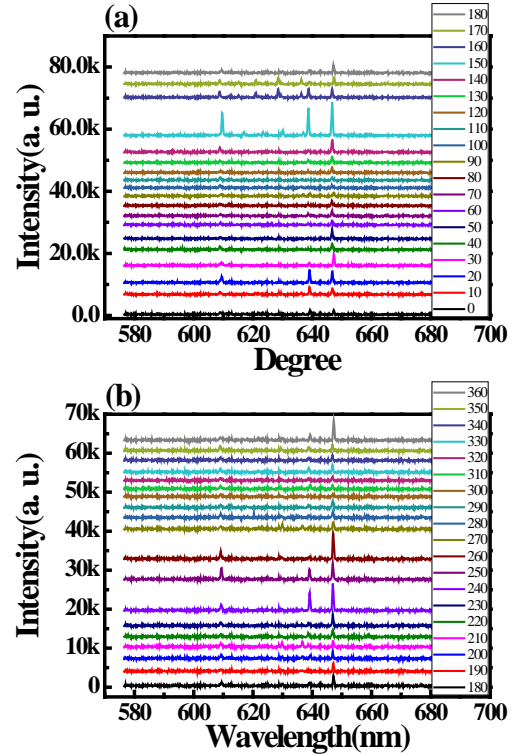


Fig. S8. Detailed spectra with different collection angles of the limaçon-spiral photonic molecule.

### c. Laser Action of the Waveguide Coupled Limaçon Microdisk and Photonic Molecule

To directly confirm the asymmetrical directional emission in experiment are formed by the internal chirality, we have fabricated an additional waveguide coupled to the limaçon of limaçon-spiral photonic molecule. The SEM image and microscope image have been shown in Fig. 5 in the main manuscript. In this figure, we just show the fluorescent microscope images of waveguide coupled limaçon microdisk and waveguide coupled limaçon-spiral photonic molecule when they are excited above the laser threshold. Here we show that threshold information. For the waveguide coupled limaçon cavity, as shown in Fig. S9, a clear threshold behavior can be seen at around  $0.7 \mu\text{J}/\text{cm}^2$ . In case of the waveguide coupled photonic molecule shown in Fig. S10, the threshold appears at around  $0.5 \mu\text{J}$ . Therefore, we can simply excite the limaçon microdisk and the limaçon-spiral photonic molecule above thresholds.



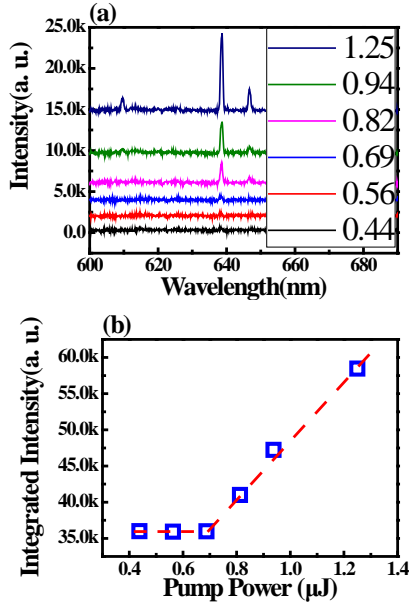


Fig. S9. (a) Detailed spectra with different pump energies of the waveguide coupled limaçon microdisk. (b) The dependence of output intensity on the pumping energy.

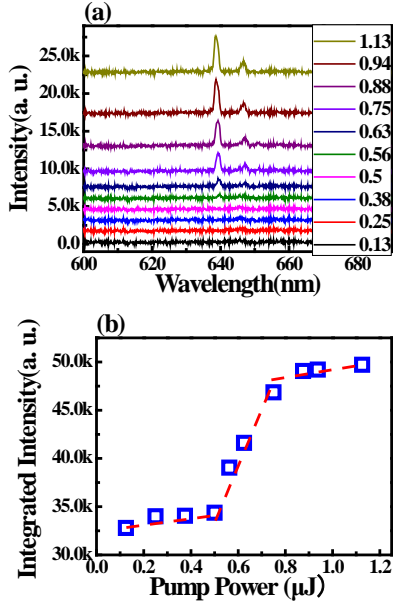


Fig. S10. (a) Detailed spectra with different pump energies of the waveguide coupled limaçon-spiral photonic molecule. (b) Dependence of output intensity on the pumping energy.

#### IV. Properties of Multiple Microdisks

In addition to the fluorescent microscope image shown as Fig. 5 in main text, here we show that the output coupling direction can be switched. All the results are shown in Fig. S11 and Fig. S12. By inserting a circular microdisk inside the limaçon-spiral photonic molecule and keeping all the other parameters, we can see that the chirality can still be formed. The only difference is that the internal chirality is dominated by CW components in Fig. S11 instead of the CCW components in Fig. 5 in the main manuscript. Interestingly, by adding another circular microdisk into the microdisk group, we can see that the output coupling direction is switched back and now the resonances inside the limaçon microdisk are dominated by the CCW components.

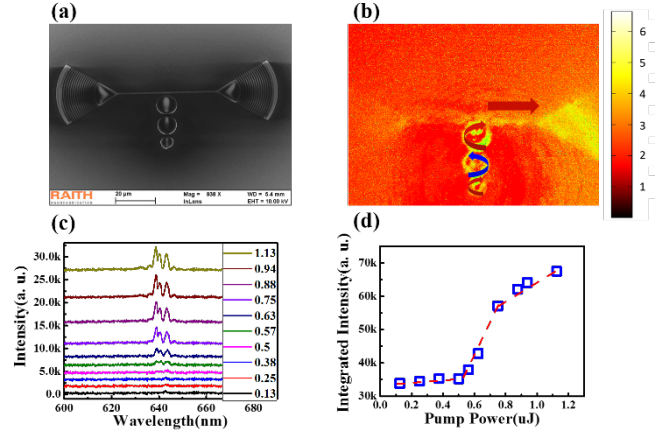


Fig. S11. (a) and (b) Top-view SEM image and corresponding fluorescent microscope image of waveguide coupled HSPM with a circular microdisk inside of them. (c) and (d) Detailed spectra with different pump energies and the output intensity as a function of pump power.

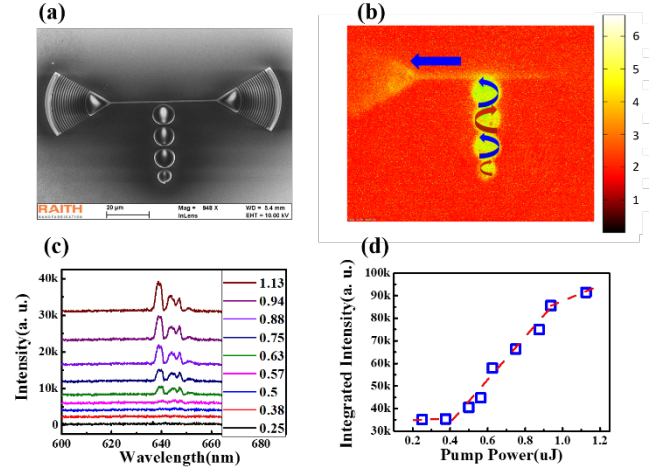


Fig. S12. (a) and (b) Top-view SEM image and corresponding fluorescent microscope image of the waveguide coupled limaçon-spiral photonic molecule with two circular microdisks inside of them. (c) and (d) Detailed spectra with different pump energies and the output intensity as a function of pump energy.

#### V. Numerical Calculations

The numerical calculations have been performed with commercial finite element methods (FEM) based software (Comsol Multiphysics 3.5a). As the thickness of microdisk is 5 times smaller than its in-plane dimensions, the microdisks are simplified to two-dimensional objects by using the effective refractive index  $n$ . The openness of the system is mimicked with a perfect matched layer to absorb the outgoing waves, and the perfect matching layer is used more than 20  $\mu$ m away from the boundary of limaçon microdisk and limaçon-spiral photonic molecule to fully absorb the outgoing waves and mimic the infinitely large space. Thus the calculated frequencies of quasi-bound states are complex numbers, and the complex eigenfrequencies ( $\omega$ ) can be normalized with  $kR = \omega R/c$  (here  $c$  is the speed of light in vacuum).

In this main text and in this supplemental information, we have shown the field pattern of limaçon microdisk and limaçon-spiral photonic molecule in Fig. S2 and Fig. 3, respectively. Fig. S13 shows the logscale plots of these field patterns. Here the emissions from the cavities can be clearly seen. In a single limaçon, two directional laser beams can be seen at far field. Once a spiral cavity is placed

close to the limaçon microcavity, the directional output of CCW waves is much stronger than the output of CW waves in Fig. S13. Following the studies in Figs. 1-3 in the main text, we thus know that optical chirality has been generated within the limaçon-spiral photonic molecule and the chirality is strongly related to their far field patterns.

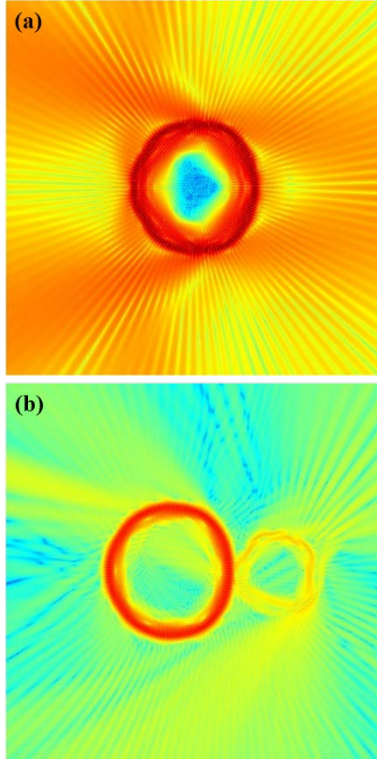


Fig. S13. The log-scale plot of field patterns. Here (a) and (b) correspond to the field patterns in Figs. 1(a) and 2(a) in the main text.

## VI. Laser Properties of the Limaçon-Spiral Photonic Molecule with a Single Nanoparticle

In Fig. 6(c) in the main text, we have shown that the changes in the far field patterns can be related to the size of a single nanoparticle. In this figure, we have compared totally five samples with the numerical simulation. The experimental results have been shown in Fig. 7 in the main manuscript. Here we show the experimental results of the total five samples. Fig. S14 (a) and (b) show the top-view scanning electron microscope images of the limaçon-spiral photonic molecule and the corresponding nanoparticle. Here the size of nanoparticle is around 100 nm. The green line and the purple line in Fig. S14(c) show the far field angular distributions of limaçon-spiral photonic molecule with and without a single nanoparticle. After attaching a single nanoparticle onto the limaçon microdisk, we can see that the emissions along  $210^\circ$  (or  $-150^\circ$ ) increase drastically. Fig. S14(d) shows the numerically simulated far field pattern. It is easy to see that the experimental results and numerically calculations match very well.

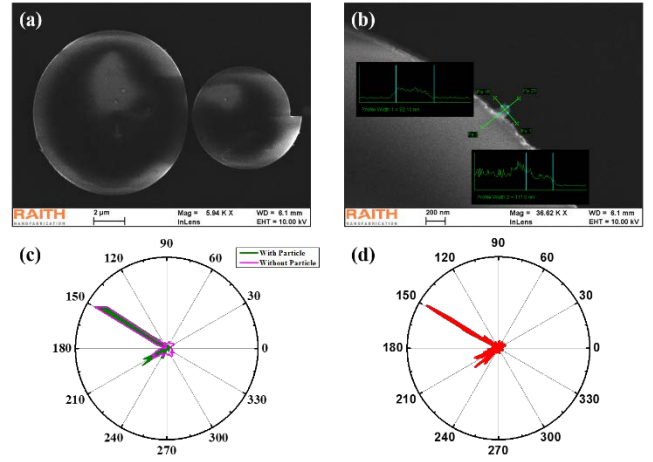


Fig. S14. (a) and (b) Top-view SEM images of the limaçon-spiral photonic molecule and the attached nanoparticle, respectively. **Here the radius of nanoparticle is around 50 nm.** (c) Far field patterns of the limaçon-spiral photonic molecule laser with and without a single nanoparticle. (d) Numerically calculated far field pattern after attaching the nanoparticle.

Fig. S15 shows the far field patterns of limaçon-spiral photonic molecule with and without a single nanoparticle. All the experimental information are the same as Fig. S14 except that the radius of nanoparticle is increased to 55 nm. Similar to Fig. S14, the changes in the far field patterns can be clearly seen after attaching the nanoparticle and the numerical simulation match the experimental results well.

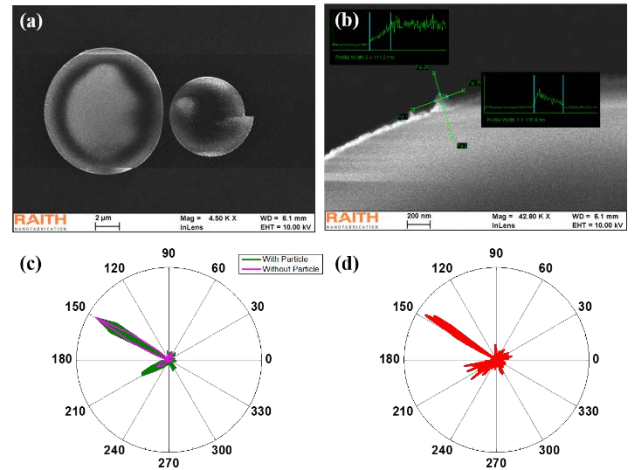


Fig. S15. (a) and (b) Top-view SEM images of limaçon-spiral photonic molecule and the attached nanoparticle, respectively. **Here the radius of the nanoparticle is around 55 nm.** (c) Far field patterns of limaçon-spiral photonic molecule laser with and without a single nanoparticle. (d) Numerically calculated far field pattern after attaching the nanoparticle.

Fig. S16 shows the far field patterns of limaçon-spiral photonic molecule with and without a single nanoparticle. Here the radius of nanoparticle is increased to  $r = 75$  nm. With the increase in  $r$ , we can see that the changes in far field pattern are more dramatic.

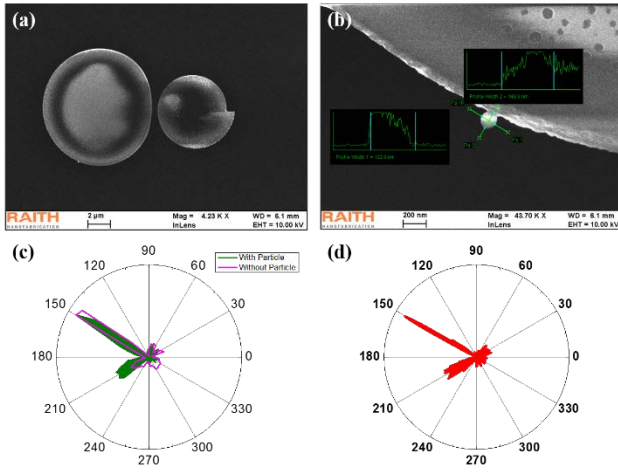


Fig. S16. (a) and (b) Top-view SEM images of the limaçon-spiral photonic molecule and the attached nanoparticle, respectively. **Here the radius of nanoparticle is around 75 nm.** (c) Far field patterns of the limaçon-spiral photonic molecule laser with and without a single nanoparticle. (d) Numerically calculated far field pattern after attaching the nanoparticle.

Fig. S17 shows the far field patterns of limaçon-spiral photonic molecule with and without a single nanoparticle. Here the radius of nanoparticle is increased to  $r = 85$  nm. As the radius is further increased, the emission along  $-150^\circ$  is also further increased.

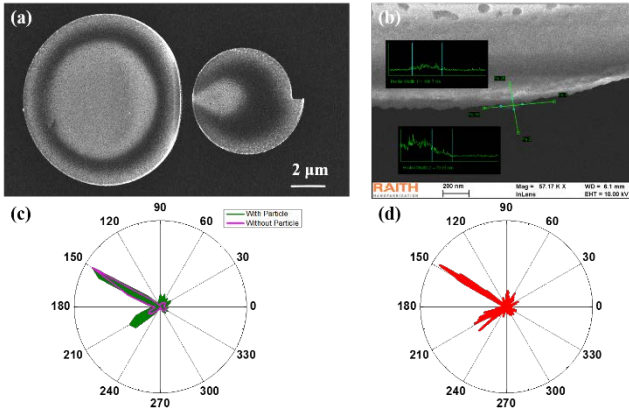


Fig. S17. (a) and (b) Top-view SEM images of the limaçon-spiral photonic molecule and the attached nanoparticle, respectively. **Here the radius of nanoparticle is around 85 nm.** (c) Far field patterns of limaçon-spiral photonic molecule laser with and without a single nanoparticle. (d) Numerically calculated far field pattern after attaching the nanoparticle.

Figure S18 shows the far field patterns of the limaçon-spiral photonic molecule with and without a single nanoparticle. As the nanoparticle is quite large here, we can see that the emission beams along  $\pm 150^\circ$  are very close now, indicating that the chirality is almost damaged by the big nanoparticle. All of these experimental results have been plotted in Fig. 6(c). We can see that the changes in far field laser emissions match the changes in chirality well and can be simply used to detect and size a single nanoparticle.

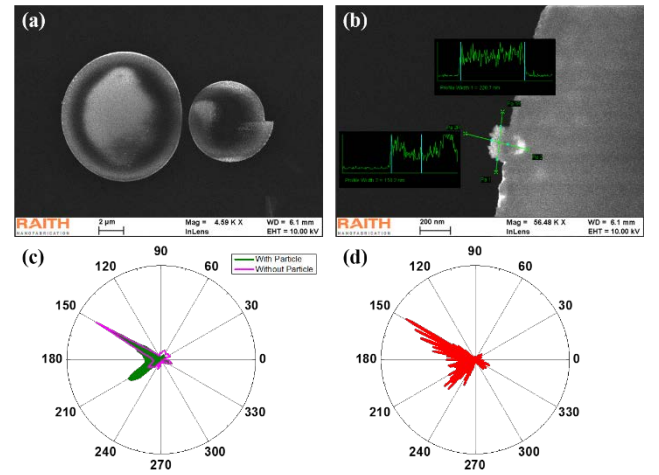


Fig. S18. (a) and (b) Top-view SEM images of the limaçon-spiral photonic molecule and the attached nanoparticle, respectively. **Here the radius of nanoparticle is around 110 nm.** (c) Far field patterns of the limaçon-spiral photonic molecule laser with and without a single nanoparticle. (d) Numerically calculated far field pattern after attaching the nanoparticle.

We then statistic the other threshold curves and the lasing spectra of the limaçon-spiral photonic molecule with the different size of nanoparticle. As shown in Fig. S19 below, the thresholds don't show an obvious dependence on the particle size. All the thresholds fall in the range from  $0.15 \mu\text{J}$  to  $0.2 \mu\text{J}$ . The slight variation is caused by the slight size deviations in different samples. This is because that the particle size is far smaller than the cavity size. In our experiment, the particle size cannot be extremely large. As Fig. 6 and Fig. S18 shown in the main manuscript and supplemental information, the nanoparticle with  $r = 110$  nm has significantly spoiled the chirality. This indicates that the upper limit of particle size should be around 110 nm. This size is still good enough to form microdisk lasers.

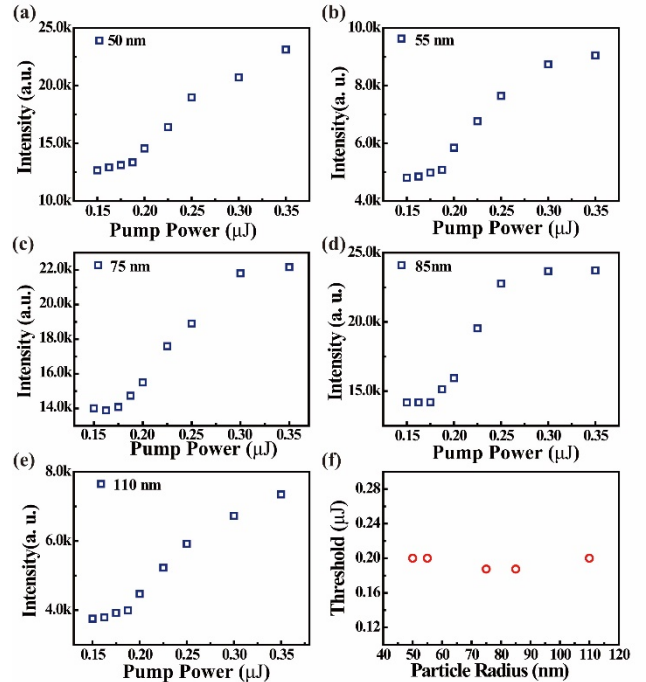


Fig. S19. (a)~(e) Threshold behavior of the limaçon-spiral photonic molecule laser after it is attached with the nanoparticle. The



radius of each nanoparticle is 50nm, 55nm, 75nm, 85nm, and 110nm, respectively. (f) The dependence of threshold on the size of the nanoparticle.

The above discussion is in the case of the single particle attached to the boundary of the limaçon cavity. We have also studied the effect of the particle on the far field pattern when it is attached to the spiral boundary (marked by red box in Fig. S20). Similar to attaching the nanoparticle to limaçon cavity, we have calculated the field patterns and far-field angular distributions of the limaçon-spiral photonic molecule as a function of the radius of the nanoparticle attached onto the spiral boundary. All the results are shown in Fig. S20 below. With the increase of nanoparticle size from 0 nm to 120 nm, both of the field patterns and the far-field angular distributions of the photonic molecules do not show any obvious changes. For a quantitative comparison, we have also calculated the chirality  $\alpha_2 = 1 - \frac{U_1}{U_2}$  with the far field angular distributions. As shown in Fig. S21, the optical chirality is well preserved with the increase of the radius of nanoparticle. Thus we can conclude that attaching a nanoparticle to the spiral boundary cannot be used to detect and size the nanoparticle.

This phenomena are understandable. In principle, the chirality is induced by the asymmetrical backscattering. As shown in Fig. S20, the sizes of the notch is orders of magnitude larger than the nanoparticle. Correspondingly, the scatterings caused by the notch are also much larger than the ones from the nanoparticle. Then the influences of the nanoparticle can be neglected. In the main manuscript, the nanoparticle attached to the limaçon is directly working on the resonant mode, whereas the notch affects the evanescent waves. As a result, the difference between the effects of nanoparticle and notch on the resonances is diminished and the nanoparticle can be detected.

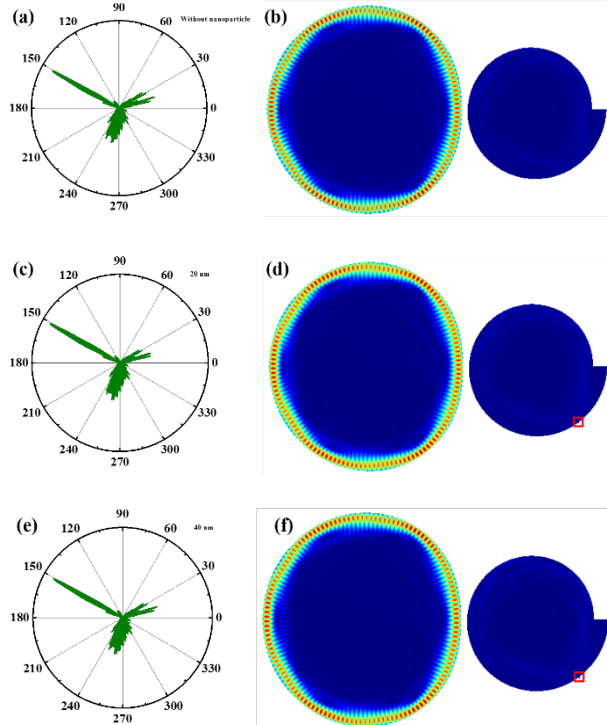


Fig. S20. Numerical results of single nanoparticles attached onto the spiral boundary. (a), (c), (e), (g), (i), (k), (m) are the far field pattern of the limaçon-spiral photonic molecule with the single nanoparticles attached to the spiral boundary. The sizes of the nanoparticles are 0 nm, 20 nm, 40 nm, 60 nm, 80 nm, 100 nm, and 120 nm, respectively. (b), (d), (f), (h), (j), (l), (n) are the field pattern of the limaçon-spiral photonic molecule.

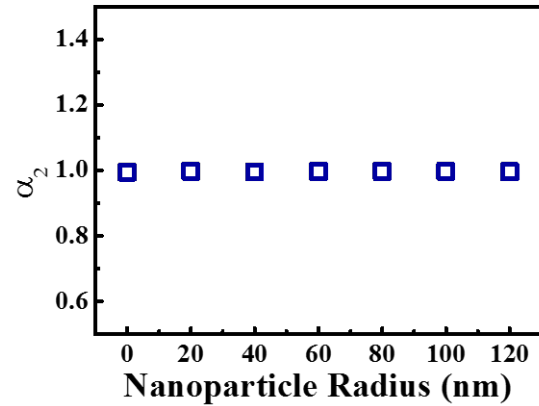


Fig. S21. The chirality  $\alpha_2$  as a function of  $r$ .